DEUTSCHES ELEKTRONEN-SYNCHROTRON
Ein Forschungszentrum der Helmholtz-Gemeinschaft

DESY 19-176
TUM-HEP-1238/19
arXiv:1911.04505
November 2019

The Schrödinger-Poisson Method for Large-Scale Structure

M. Garny
Physik Department T31, Technische Universität München, Garching

T. Konstandin, H. Rubira
Deutsches Elektronen-Synchrotron DESY, Hamburg

ISSN 0418-9833

NOTKESTRASSE 85 - 22607 HAMBURG

DESY behält sich alle Rechte für den Fall der Schutzrechtserteilung und für die wirtschaftliche Verwertung der in diesem Bericht enthaltenen Informationen vor.

DESY reserves all rights for commercial use of information included in this report, especially in case of filing application for or grant of patents.

To be sure that your reports and preprints are promptly included in the
HEP literature database
send them to (if possible by air mail):

DESY Zentralbibliothek Notkestraße 85 22607 Hamburg Germany	DESY Bibliothek Platanenallee 6 15738 Zeuthen Germany

arXiv:1911.04505v2 [astro-ph.CO] 3 Apr 2020

Physik Department T31, James-Franck-Straße 1,
Technische Universität München, D–85748 Garching, Germany

Deutsches Elektronen-Synchrotron DESY,
Notkestraße 85, D-22607 Hamburg, Germany

$$\frac{}{} \qquad \frac{}{} \qquad \frac{}{}\frac{}{} \qquad\qquad \frac{}{}$$

$$\int \frac{}{}$$

$$\int \frac{\quad}{\quad} \qquad \left[\quad \frac{\quad}{\quad} \right]$$

$\mathbf{l}$ $\mathbf{l}$ $\mathbf{l}$ $\mathbf{l}_i$ $\mathbf{l}_j$ $\mathbf{l}$

$\frac{\quad}{\quad}$ $\mathbf{l}$ $\mathbf{l}$ $\mathbf{l}$

$$\frac{\quad}{\quad}$$

$$-\sum^{\text{bodies}}$$

1

$$\frac{}{} \int \quad \left[- \quad \right]$$

$$\int$$

$$\frac{\left[\frac{\mathbf{x} \quad \mathbf{y}^{2}}{2_{x}} \qquad \frac{\mathbf{p}\,\mathbf{y}}{} \right]}{\frac{D}{2} \qquad\qquad \frac{D}{4}}$$

$$- \qquad \frac{}{}$$

$$\sqrt{\qquad\qquad} \qquad \mathbf{k}$$

$$\int \qquad \int \qquad \int$$

$$\int \qquad \mathbf{x}\,\mathbf{k}$$

$$\int$$

$$\int$$

$$\int$$

$\frac{i}{\hbar}\int_{\eta}^{\eta+\Delta\eta}$

$\int_{\eta}^{\eta+\Delta\eta} \qquad \frac{\kappa}{2}$

$$\Big(\quad - \quad \Big)$$

$$\Bigg(\quad \int \qquad \Bigg)$$

$\lesssim$

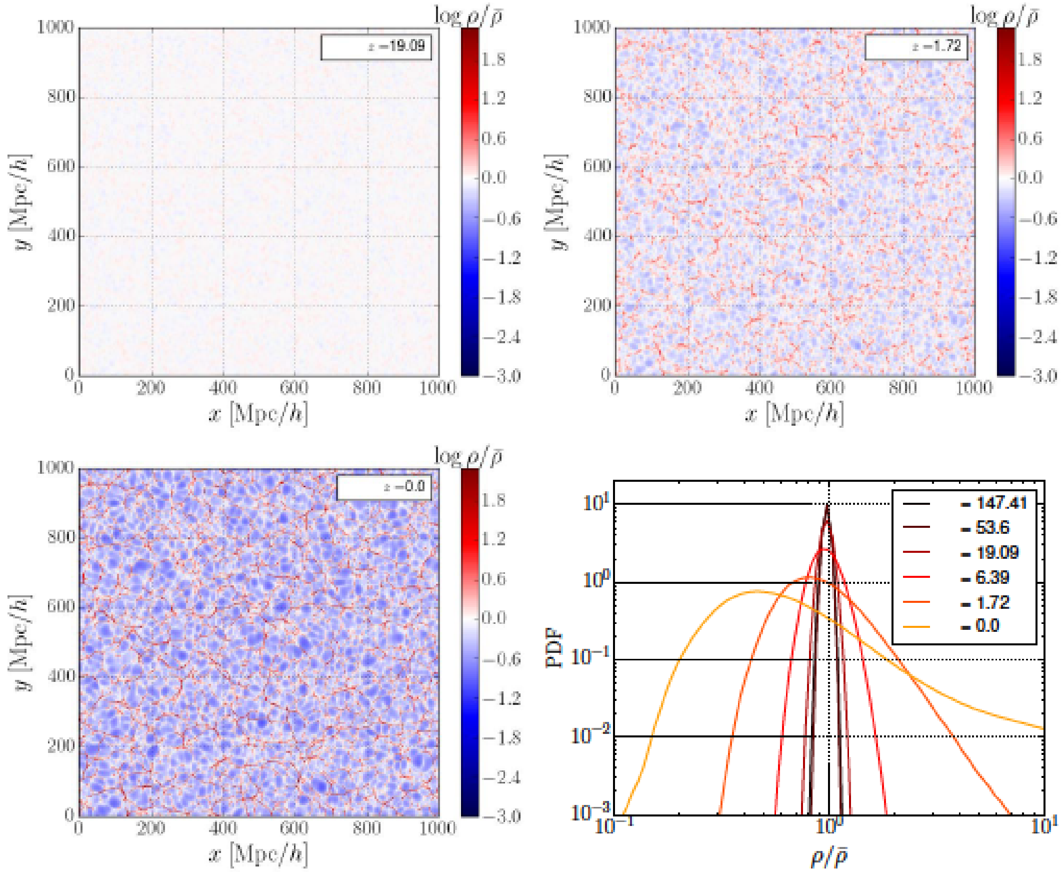

Figure 1. Density contrast at three different redshifts ($z = 19.09$, $z = 1.72$ and $z = 0$) for the 2D Schrödinger-Poisson system for $L = 1000$ Mpc/h, $\kappa_0 = 1$ Mpc$^2/h^2$ and $N = 8192$. In the bottom-right, the density PDF at various redshifts is shown.

smoothing length 2 Mpc/h. For a given set of simulation parameters, the PDF without filtering has similar shape as the smoothed one, apart from the high-density tail.

The matter power spectrum is shown in figure 2. The time evolution of the SP system imprints three different types of features on the power spectrum, which we list below:

1. A strong exponential (Jeans) suppression at small scales (section 4.1);
2. Sampling noise on large scales that were not present in the initial conditions (section 4.3);
3. A slight loss of power for all modes at low redshift (section 4.2).

The first effect is a physical property in fuzzy dark matter models related to the Jeans scale (2.16), but should be considered as a systematic limitation when applying the SP method to describe the phase space evolution of cold dark matter. Notice that,

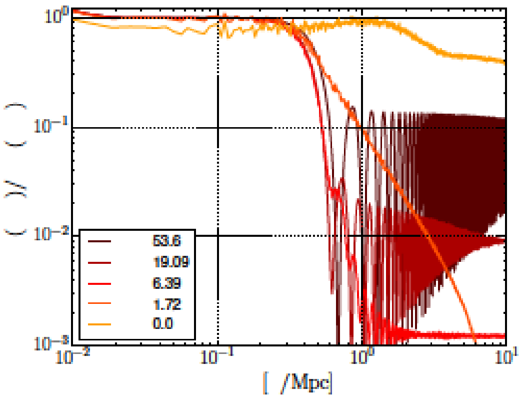

Figure 2. Matter power spectrum divided by the linear power spectrum at redshifts $z = 0, 1.72, 6.39, 19.09, 53.6$.

at late time, the Jeans scale does not suppress all power on small scales. So non-linear growth seems to be less affected than one would expect from the linear analysis of the system. As shown below, the second item is essentially analogous to sampling noise in N-body simulations, which is related to the finite number of modes. The third feature has already been recognized in the context of fuzzy dark matter [40], and is a systematic error of the (discretized) SP method for both fuzzy and cold dark matter.

4 The systematics of the Schrödinger-Poisson method

In this section, we quantify each one of the three systematics effects mentioned above and evaluate their dependence on the simulation parameters, including the box size L, the number of lattice points in each dimension N, and the phase space resolution controlled by the value of $\hbar$. Since the latter enters in the rescaled SP equations (2.19) only via the function $\kappa(\eta)$ (see (2.17)), we trade $\hbar$ for κ_0, the present value of κ. We study variations around the fiducial values $L = 1000$ Mpc$/h$, $N = 4096$ and $\kappa_0 = 1$ Mpc$^2/h^2$, which we found to be parameters that describe the BAO peak reasonably well while requiring a feasible amount of computational time (see appendix D). Furthermore, we use a fixed initial redshift $z = 147$. For comparison, the original work [33] used $N = 256$ and $L = 150$ Mpc$/h$ in 2D.

In figure 3, we show the dependence of the PDF on the simulation parameters (N, on the left; L in the middle and κ_0 on the right). In the strict limit of (infinitely) *cold* dark matter, the PDF is not expected to converge uniformly (without any coarse-graining) when increasing N/L, since smaller and smaller structures are resolved [55]. However, for the Schrödinger-Poisson system with fixed $\hbar$ (i.e. fixed κ_0), the Jeans scale acts as a coarse-graining length which should improve convergence. We find that increasing the number of lattice points enhances the deviation from a Gaussian distribution, and increases the tails of the PDF. Nevertheless, for $N = 8192$ the PDF

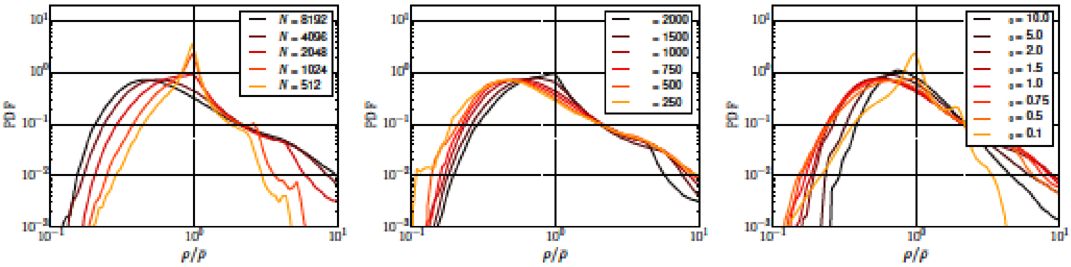

Figure 3. Dependence of the PDF of the matter density on the simulation parameters: For different grid sizes N on the left; for different box sizes L (in units of Mpc$/h$) in the middle, and for different $\kappa_0 \propto \hbar$ (in units of Mpc$^2/h^2$) on the right. We use a top-hat filter in position space with a smoothing scale of $2\,\mathrm{Mpc}/h$.

did not converge yet. As mentioned before, for the PDF we apply a top-hat filter in position space with smoothing length $2\,\mathrm{Mpc}/h$ (see also appendix E, in which we explore the convergence for the 1D case). Decreasing the box size L with N fixed also improves the resolution of the non-linear modes, while increasing the box size too much leads to a loss of resolution. Decreasing κ_0 leads to similar effects that are accompanied by an overall loss of power in the fluctuations. Larger values of κ_0, in turn, increase the quantum pressure what also suppresses non-linearities. For intermediate values of κ_0 the result is relatively stable. While no clear picture emerges for the PDFs, the role of the different parameters will become more clear in the following when we study the power spectrum.

4.1 Jeans suppression

The exponential loss of power at some scale k_{fall} related to the Jeans scale (2.16) is a characteristic property of the SP system. The Heisenberg uncertainty principle inhibits the formation of structures that are smaller than the Jeans scale. In the context of using the SP method to describe cold dark matter, the Jeans suppression has to be considered as a source of systematic errors. In the left panel of figure 2, we can see that shortly after initializing the simulation, the Jeans suppression strongly affects the power spectrum above around $\sim 1h/\mathrm{Mpc}$. To quantify the scale k_{fall} where the exponential suppression appears, we define it to be the largest mode for which the ratio of the power spectrum to the corresponding linearly evolved ΛCDM input power spectrum $P_{lin}(k, z)$ is smaller than 90%

$$k_{\mathrm{fall}} = \min(k) \quad \text{for which} \quad \frac{P(k, z_{ref})}{P_{lin}(k, z_{ref})} < 0.9\,. \tag{4.1}$$

We measure this scale at $\eta = -4$ ($z_{ref} = 53.6$), when the other systematic effects are still irrelevant and the system already had enough time to develop Jeans suppression after being initialized with a ΛCDM spectrum at $z = 147$. For the fiducial simulations used here we find $k_{\mathrm{fall}} \simeq 0.3h/\mathrm{Mpc}$.

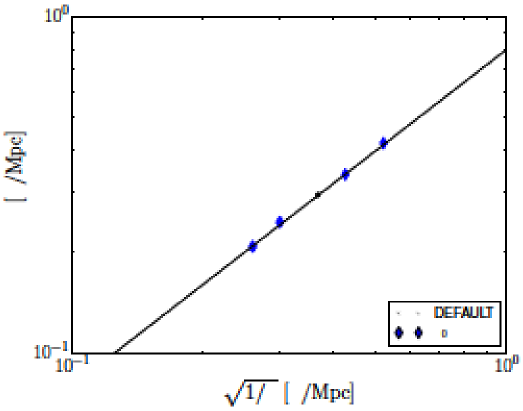

Figure 4. Schrödinger-Poisson systems in the linear regime feature a characteristic length scale below which structures are strongly suppressed due to the uncertainty principle. We quantify this scale in Fourier space as k_{fall}, which we found to be proportional to $\sqrt{1/\kappa}$. The diamonds correspond to a variation of κ_0 around its fiducial value (shown by the black point). The line corresponds to $k_{\text{fall}} = 0.8\sqrt{1/\kappa(z_{ref})}$.

In figure 4, we show the dependence of this cutoff scale on κ_0, which we find to be the single parameter that affects k_{fall}. Reducing κ_0 allows structures on smaller scales to form and therefore shifts the exponential suppression to larger wavenumbers, as expected. Parametrically, we find

$$k_{\text{fall}} \propto \frac{1}{\sqrt{\kappa}}, \tag{4.2}$$

which implies a slight time-dependence of this scale (in comoving momenta) of $\kappa^{-1/2} \propto \exp(\eta/4) \propto a^{1/4}$. This confirms the interpretation as suppression related to the Jeans scale (2.16). Note that the interpretation of the wave-function obtained from the SP equations in terms of the Madelung representation, and the associated quantum pressure, are potentially ambiguous at these scales, as discussed above. Nevertheless, the Jeans analysis appears to predict the correct scaling of k_{fall} at early redshifts. At low redshift, additional structure on smaller scales starts to form as mentioned before.

4.2 The amplitude problem

The simulations show another effect that is a little bit more subtle and harder to understand. It is a loss of power towards the end of the simulation. This loss of power is evident for the smallest wavenumbers where one would expect linear evolution. In figure 5, we display the evolution of the power spectrum as a function of η for three different modes (continuous lines). We compare with the linear evolution (dashed lines). It is possible to visualize a specific time, close to the end of the simulation ($\eta = 0$) for which each of the perturbation modes decouples and stops growing. The amplitude loss is essentially given by the amount of linear growth after this decoupling.

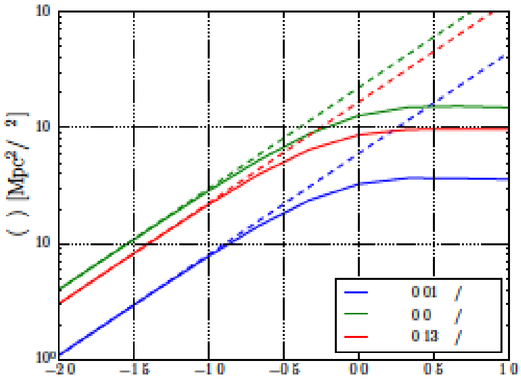

Figure 5. Amplitude loss of the (2D) power spectrum versus time $\eta = \ln(a)$, for three different wavenumbers. Solid lines show the simulation result and dashed lines the expected linear growth. The perturbations decouple and stop growing at a particular time, which depends on the simulation parameters (see main text, the plot is for our fiducial choice).

To quantify this loss in power, we fit a straight-line coefficient A^2 to the ratio of the measured $P(k)$ to the rescaled power spectrum of the initial conditions $P_{\rm init}$ as expected by the linear growth function (for the modes $k < k_{\rm fall}$)

$$A^2 = \left\langle \frac{P}{P_{\rm init,rescaled}} \right\rangle_{k<k_{\rm fall}} . \tag{4.3}$$

In the left panel of figure 6, we display the evolution of A^2 with time η. For our fiducial set of simulation parameters, the power loss sets in at $\eta \simeq -2$ ($z \simeq 6.4$), when the non-linear evolution becomes more relevant. For larger N, the SP power loss is less than 2% up to $\eta \simeq -1$ ($z \simeq 1.7$).

In the right panel of figure 6, we display the dependence of the amplitude loss at $z = 0$ on the simulation parameters N, L, and κ_0. We find that the amplitude loss depends only on the combination $\kappa_0 N/L$. It has the unit of a distance, and we find the critical length scale above which the amplitude loss effect becomes irrelevant to be

$$\frac{\kappa_0 N}{L} \gtrsim l_{\rm crit,0} \simeq 10\,{\rm Mpc}/h\,. \tag{4.4}$$

This can also be written as a condition on the lattice spacing L/N,

$$\frac{L}{N} \leq \frac{\kappa_0}{l_{\rm crit,0}} = \frac{\hbar}{m}\frac{1}{H_0\, l_{\rm crit,0}}\,. \tag{4.5}$$

In Ref. [32] it was speculated that the lattice spacing L/N has to be smaller than the de Broglie wavelength $\lambda = \hbar/mv$, where v is the typical group velocity of a wave

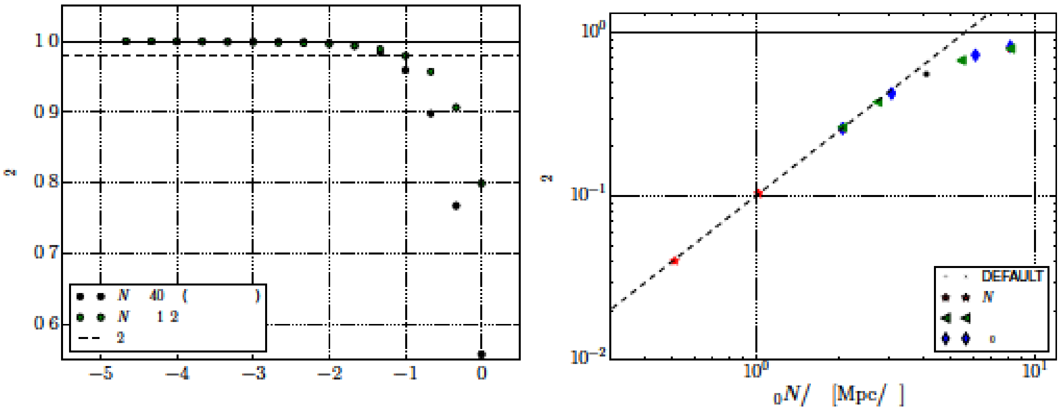

Figure 6. Left: Amplitude loss versus time η for the fiducial choice of parameters (black) and for a higher resolution ($N = 8192$, green). Right: Dependence of the amplitude loss at $z = 0$ on the combination of the simulation parameters $\kappa_0 N/L$. The different symbols correspond to variation of either N, L or κ_0 while keeping the other parameters fixed at their fiducial values. The dashed line corresponds to the scaling $A^2 \propto (\kappa_0 N/L)^{4/3}$, which is inferred in the text.

packet. This suggests that the length scale l_{crit} is related to the velocity

$$l_{\text{crit}} = \frac{1}{Ha}\sqrt{\langle \mathbf{u}^2 \rangle}\,, \tag{4.6}$$

with $\mathbf{u}$ determined from the wave-function as given by (2.13). Here, we defined l_{crit} not at redshift zero but at general redshift as it would be measured on the lattice without introducing additional factors a or H according to (2.13), see discussion below.

To obtain the value of l_{crit} applicable to cold dark matter, one has to extrapolate the numerical results for $\langle \mathbf{u}^2 \rangle$ to $\hbar \to 0$ since $\mathbf{u}$ also suffers from a suppression just as the power spectrum. We find that $l_{\text{crit},0} \simeq 15\,\text{Mpc}/h$. Alternatively, one can estimate l_{crit} in linear theory. Using the linear growing mode relation $\mathbf{u} = -aH\nabla\delta/\Delta$ for the EdS background considered here gives

$$l_{\text{crit}}^{\text{lin}} = \left(\int \frac{d^3k}{(2\pi)^3} \frac{P_{lin}(k,z)}{k^2} \right)^{1/2}\,, \tag{4.7}$$

which yields $l_{\text{crit},0}^{\text{lin}} \simeq 10\,\text{Mpc}/h$. This fits well with the scale inferred from the behavior of the power loss.

Here, a couple of comments are in order. First, $\mathbf{u}$ relates to the average peculiar velocity in the fluid and has no direct connection to the microscopic motion of the particles or wave packets. Hence, $\hbar/(m\sqrt{\langle \mathbf{u}^2 \rangle})$ strictly speaking does not represent the de Broglie wave length. Nevertheless, it appears to provide a valid estimate of the amplitude loss effect. In fact, the suppression of the power spectrum probably arises from the fact that a maximal velocity exists on the lattice [38], and is probably not intrinsic of our numerical scheme. Due to the spatial discretization $\nabla\phi/\hbar < \pi N/L$ which turns into the bound

$$\frac{|\mathbf{u}|}{aH} < \kappa\pi\frac{N}{L}\,. \tag{4.8}$$

So the relation (4.5) can be read as a requirement on the lattice spacing to resolve all relevant velocities in the simulation. We tested this by studying the relative phases between neighboring grid points. In Fig. 7 we show the suppression factor A^2, the average of the relative phases and the fraction of large relative phases ($> \pi/4$). The suppression happens in tandem with the occurrence of large relative phases. As a cross-check we also confirmed that energy is approximately conserved in our simulations (see Appendix B) which would indicate a failure of our numerical integration of the equation of motion.

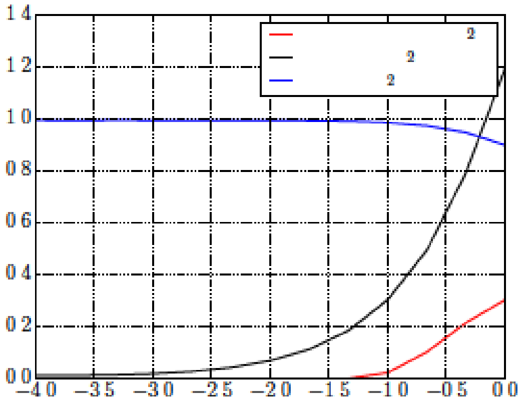

Figure 7. The plot shows the suppression factor A^2, the average of the relative phases and the fraction of large relative phases ($> \pi/4$) versus time.

Second, note that the quantity $\langle\mathbf{u}^2\rangle$ is dominated by long wavelength modes. In linear approximation, this is apparent in Fourier space, noticing that $|\mathbf{u}^2| \simeq |\delta|^2(aH)^2/k^2$. The integral over the corresponding power spectrum in (4.7) is dominated by modes $k \lesssim 0.1h/\mathrm{Mpc}$. This property fits quite well with the observation that the suppression in the power spectrum is rather wavenumber-independent.

Third, we find that at finite redshift (4.5) is generalized to

$$\frac{L}{N} \le \frac{\kappa}{l_{\rm crit}} = \frac{\hbar}{m}\,\frac{1}{a^2\,H\,l_{\rm crit}} \simeq \frac{\hbar}{a\,m\sqrt{\langle\mathbf{u}^2\rangle}}\,, \tag{4.9}$$

Notice that the time-dependence in (4.7) implies $l_{\rm crit} \propto a$ in the linear regime and hence $\kappa/l_{\rm crit} \propto a^{-3/2}$. Therefore, the amplitude loss sets in when

$$a \ge a_{\rm crit} \simeq \left(\frac{\kappa_0 N/L}{l_{\rm crit,0}}\right)^{2/3}\,. \tag{4.10}$$

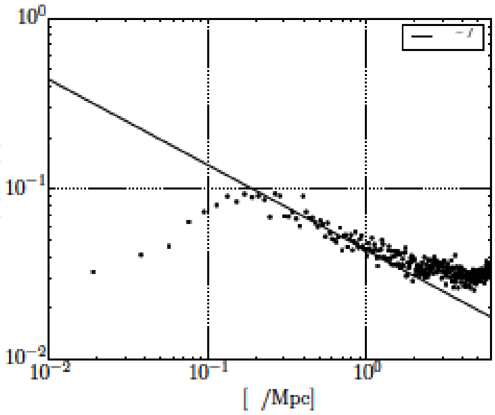

Figure 8. Sampling variance of the power spectrum at $z = 0$ obtained from 64 realizations, normalized to the power spectrum as a function of the wavenumber. We also show a line that corresponds to the expected scaling based on the number of Fourier modes in 2D.

twofold: First, the computational time increases because the argument of potential rotations U_V becomes larger, which requires to reduce the time step [see (2.17)]. Second, lowering κ_0 makes the amplitude loss problem described above more severe. The best alternative would then be to reduce κ_0 while increasing N, at the cost of more demanding simulations.

In order to mitigate the loss of power at late times, one can either increase κ_0 or make the lattice spacing L/N smaller. The first alternative comes with the price of an exponential suppression at a smaller k_{fall}. Increasing N increases the computational cost (see appendix D), while decreasing L increases the sampling noise. For the 2D simulation with $L = 1000$ Mpc$/h$, $\kappa_0 = 1$ Mpc$^2/h^2$ and $N = 8192$, we measured the amplitude loss, Jeans suppression and sampling noise at $z = 0$, to be

$$A^2 = 0.8\,, \tag{4.12}$$

$$k_{\text{fall}} = 0.3\,h/\text{Mpc}\,, \tag{4.13}$$

$$\sigma/P \sim 10\%\,. \tag{4.14}$$

In this context, it is interesting to explore the 1D case, for which we can substantially increase the resolution (see appendix E). In that case, we can decrease the loss in power for the SP system for $N = 80.192$ down to the percent level.

Instead of increasing $\kappa_0 N/L$, one may wonder whether it is possible to apply a correction that compensates for the amplitude power loss. The simplest possibility is to rescale the power spectrum by $1/A^2$. However, the extent to which this naive rescaling captures non-linear growth is unclear. Nevertheless, we followed this approach to investigate the correlation function around the BAO peak (see below). Alternatively, one could run the simulation somewhat longer in the hope that this captures the non-linear effects better than just a rescaling. However, it turns out that this only works

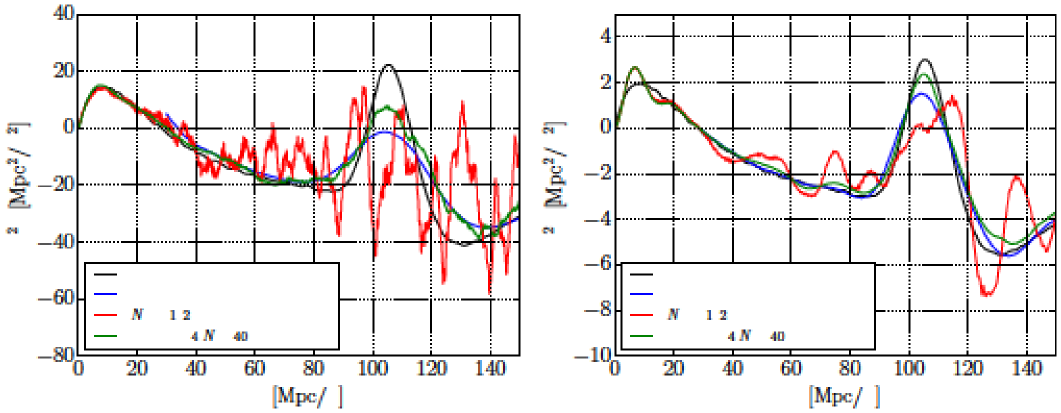

Figure 9. Correlation function $x^2\xi(x)$ for redshift $z = 0$ (left) and $z = 1.72$ (right). We show the SP result obtained from averaging over 64 simulations with fiducial parameters, from a single simulation with parameters as in figure 2, in linear theory and for Zel'dovich approximation.

figure 10, we display the overdensity field for three different redshifts in a slice of the simulation volume, after calculating the mean of 10 bins along the z axis.

In the bottom right panel of figure 10, the PDF of the density field for different redshifts is shown. Even though the PDF departs from its initial shape, developing some skewness and kurtosis, it is still far from developing the non-linear shape found in 2D (see e.g. figure 2).

The power spectrum is shown in figure 11. It features Jeans-like suppression at large k as in 2D, as well as an overall amplitude loss at low redshift. For the 3D simulation, the parameters characterizing the overall power loss and the Jean suppression scale defined in section 4 are found to be (at $z = 0$)

$$A^2 = 0.6\,, \tag{5.1}$$

$$k_{\rm fall} = 0.15\,h/{\rm Mpc}\,. \tag{5.2}$$

Notice that the power loss in terms of A^2 is in accordance with the parametric dependence on simulation parameters identified in the 2D case. In particular, for the 3D simulation $\kappa_0 N/L \simeq 3.4$ Mpc$/h$, which implies that $l_{\rm crit}$ is close to the 2D value.

In order to obtain acceptable values of the power loss, the box size has been reduced and κ_0 increased compared to 2D. The latter leads to a smaller $k_{\rm fall}$. In principle, one could increase $k_{\rm fall}$ while keeping A^2 fixed by decreasing κ_0 and L. However, this is not possible since the BAO peak has to fit into the box. Ultimately, one will have to keep the box size fixed and increase N. The sampling noise is substantially reduced compared with the 2D case, because the number of modes for a fixed momentum $|k|$ is larger and scales as $(k\,L)^2$.

The correlation function (see figure 12) extracted from a single realization is substantially less affected by noise as compared to 2D. As before, we rescaled $\xi(x)$ ex-

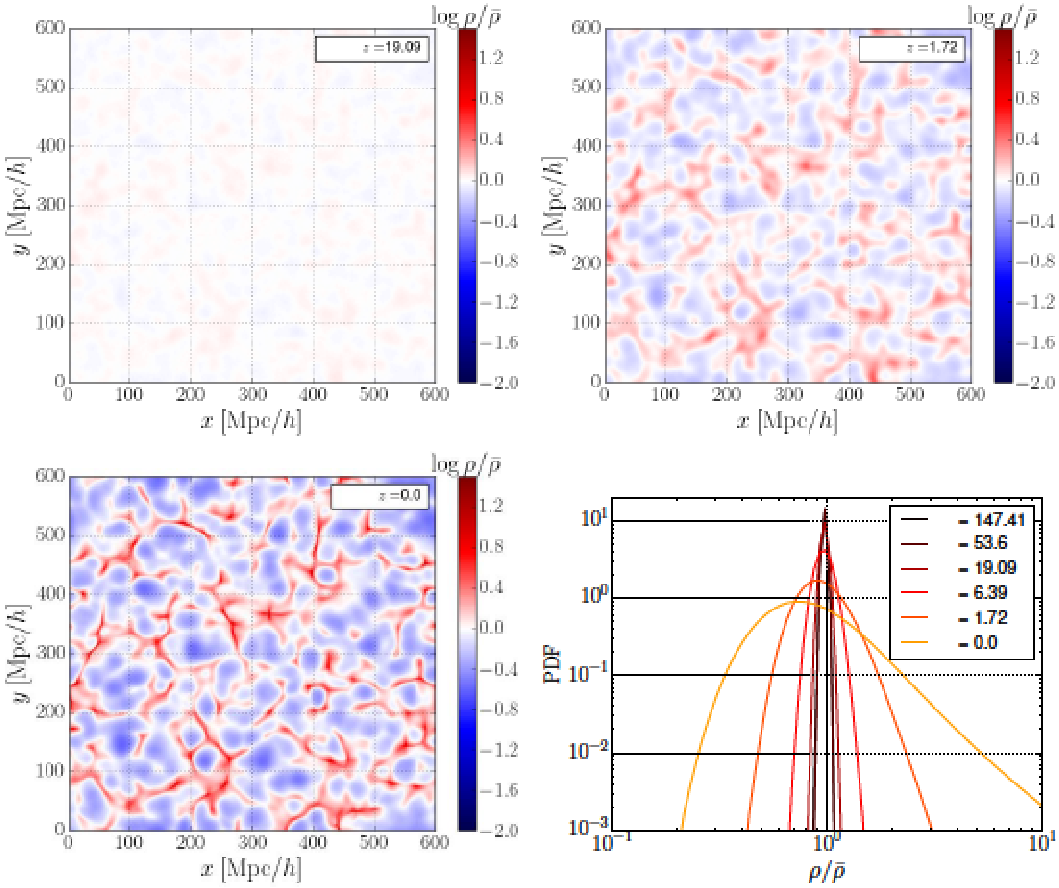

Figure 10. Density field at three different redshifts ($z = 19.09$, $z = 1.72$ and $z = 0$) for the 3D Schrödinger-Poisson system. We projected the density field taking the mean of 10 slices. In the bottom right panel, the PDF of the density field at various redshifts z is shown.

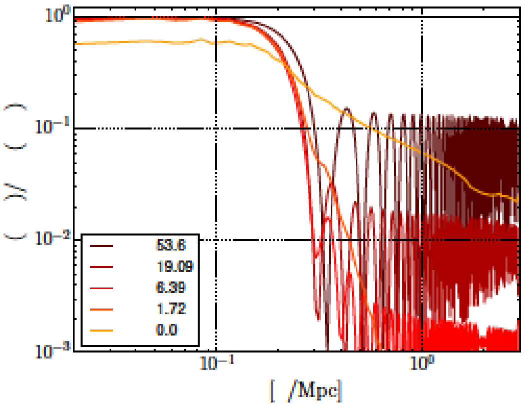

Figure 11. Power spectrum obtained from a 3D SP simulation at various redshifts z, using $L = 600$ Mpc $/h$, $N = 512$ and $\kappa_0 = 4\,\mathrm{Mpc}^2/h^2$.

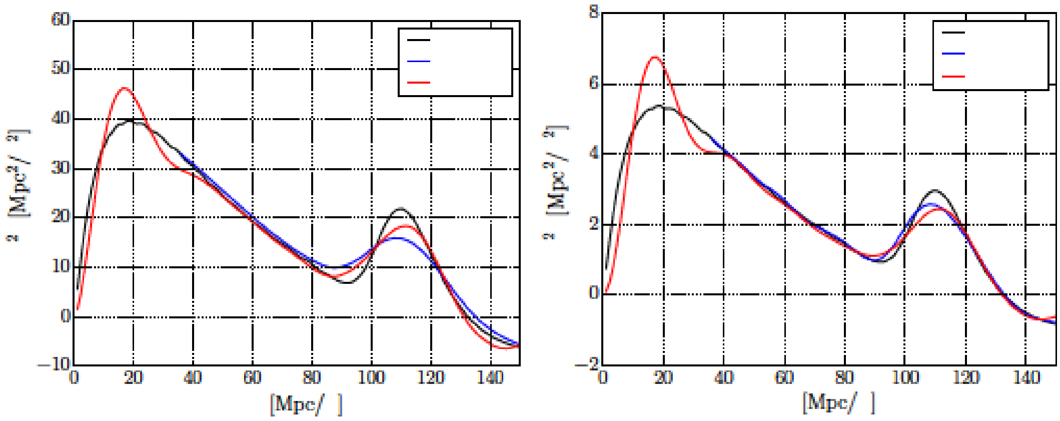

Figure 12. Correlation function for the 3D SP simulation at $z = 0$ (left) and $z = 1.27$ (right).

tracted from the simulation by $1/A^2$ at each redshift. The result is then found to be relatively close to the Zel'dovich approximation for $z = 1.72$, while a slight lack of BAO broadening is visible at $z = 0$, similar to the 2D case.

6 Conclusion

We studied the growth of large-scale structure at BAO scales using the Schrödinger-Poisson approach for cold dark matter. The main question is if large-scale simulations, competitive with N-body simulations, are feasible in this setup. The appeal of a second independent approach to large-scale structure is that the Schrödinger-Poisson method comes with a different methodology for initial conditions, dynamics, no gravitational softening and hence different systematic uncertainties. Besides, it makes higher moments of the phase space distribution function and velocity correlation functions more readily available. We identified three systematic effects (for most parts already seen previously in refs. [31, 40, 48]) and studied their parametric dependence on the simulation parameters. There is a Jeans damping scale, an overall suppression of the amplitude (due to a lack of resolution of the wave packets) as well as sampling noise. We provide a quantitative criterion to determine the redshift after which amplitude suppression sets in, and find a particular combination of simulation parameters it depends on. In order to avoid this effect, the simulation parameters should obey

$$\frac{L}{N} \leq \frac{\kappa}{l_{\text{crit}}} \simeq \frac{\hbar}{a\, m \sqrt{\langle \mathbf{u}^2 \rangle}} \,. \tag{6.1}$$

We interpret this criterion in terms of an effective de Broglie wavelength and the existence of a maximal velocity in the simulation.

The main challenge in 3D is to clearly separate all the occurring scales in the simulations (see figure 13). Ideally, the Jeans scale should be substantially smaller

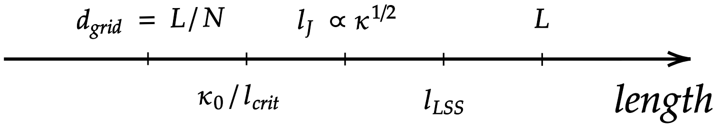
$d_{grid} = L/N$
$l_J \propto \kappa^{1/2}$
L
κ_0 / l_{crit}
l_{LSS}
length

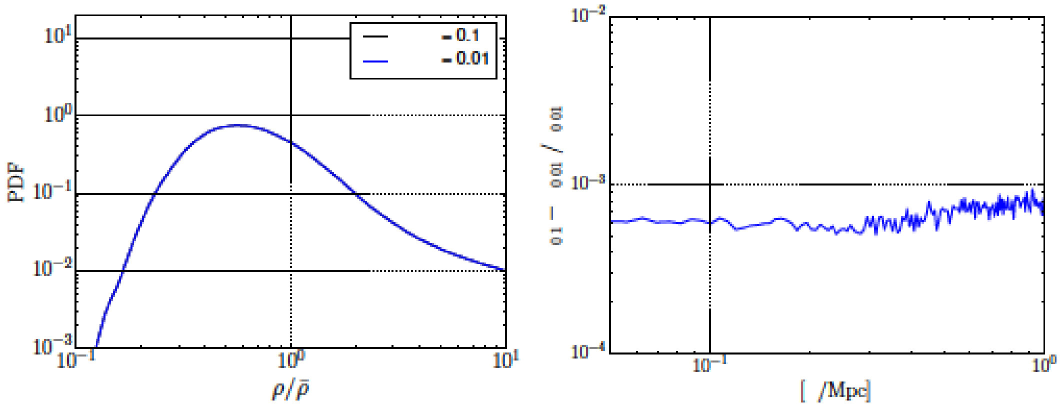

Figure 14. Convergence of the SP solution when reducing the time step. In the left, the PDF obtained for $\theta_{\max} = 0.01$ and $\theta_{\max} = 0.1$ is shown. The PDFs overlap, being indistinguishable. In the right, the relative difference in the power spectrum is shown.

using $\theta_{\max} = 0.01$ instead. In the left panel, both PDFs overlap. In the right panel, we show the relative difference of the density power spectrum, which is below 10^{-3} over the entire range of scales considered in this work. The relative difference of the wave-function ψ is of the order of $\sim 10^{-6}$. We conclude that using $\theta_{\max} = 0.1$ is sufficient to guarantee numerical stability.

B Energy conservation

As proposed in [37] we also perform the Layzer-Irvine test of energy conservation in our simulations. In our setup, the kinetic and potential energies are naturally defined as

$$K = -\frac{\kappa}{2}\int \psi^* \Delta\psi\,, \tag{B.1}$$

$$W = \frac{1}{2}\int \bar{V}\,\psi^*\psi\,. \tag{B.2}$$

Energy conservation is then spoiled by the explicit time dependence of κ in K and also in $\bar{V}$ (see Eq. (2.20)). This yields the relation

$$\partial_\eta(K+W) = -\frac{1}{2}K + \frac{1}{2}W\,. \tag{B.3}$$

This motivates the definition

$$\delta_K = \frac{\partial_\eta(K+W) - W/2 + K/2}{K}\,. \tag{B.4}$$

In Fig. 15 we show δ_K for 1D ($L = 1000$ Mpc$/h$, $N = 16384$ and $\kappa_0 = 1$ Mpc$^2/h^2$), 2D ($L = 1000$ Mpc$/h$, $N = 4096$ and $\kappa_0 = 1$ Mpc$^2/h^2$) and 3D ($L = 1000$ Mpc$/h$, $N = 256$ and $\kappa_0 = 1$ Mpc$^2/h^2$) simulations.

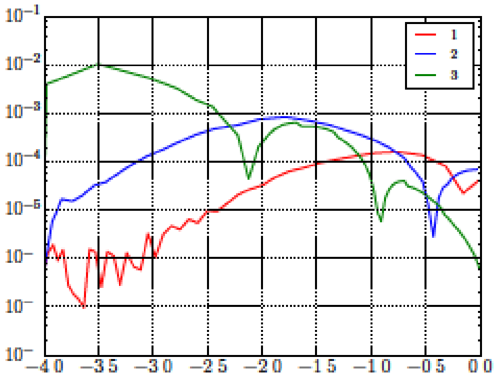

Figure 15. The plot shows δ_K as a function of time for simulations in 1D, 2D and 3D. The Layzer-Irvine test is passed ($\delta_K \ll 1$) in all cases. See text for the parameters of the simulations.

C Initialization redshift

In figure 16 we show the impact of initializing the SP evolution at two different redshifts $z_{\rm init} = 147.4$ and $z_{\rm init} = 53.6$ using $L = 1000$ Mpc$/h$, $N = 8192$ and $\kappa_0 = 1$ Mpc$^2/h^2$. The initial redshift has a relatively strong influence on the PDF at $z = 0$. The relative difference of the matter power spectrum is below 2% for $k \lesssim 0.25h/$Mpc. N-body simulation results using Zel'dovich approximation as initial conditions also find similar discrepancies [13].

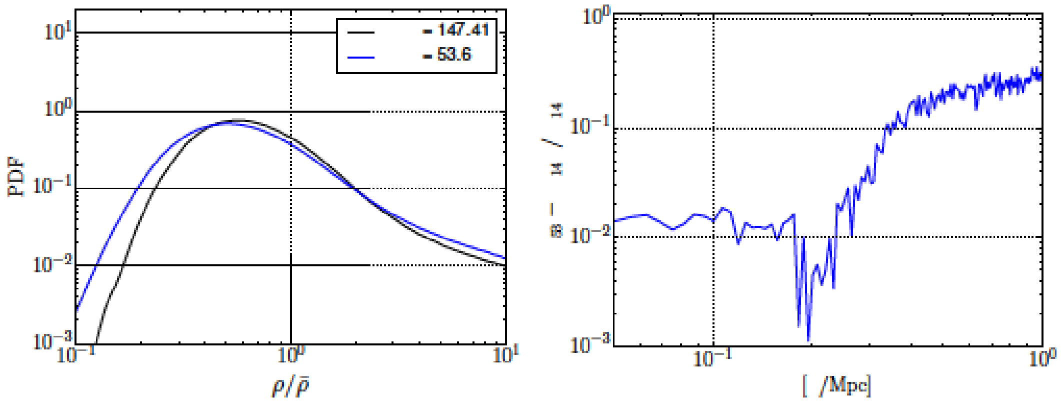

Figure 16. Left: PDF for the matter density field at $z = 0$ using redshifts $z_{\rm init} = 147.4$ and $z_{\rm init} = 53.6$. Right: Relative difference of the matter power spectrum at $z = 0$ obtained for the two initial redshifts $z_{\rm init}$.

D Computational time

In this appendix, we comment on the computational CPU time required for the Schrödinger-Poisson code. All the simulations were performed on the DESY Theory Cluster. For the Fourier transformations, we used the FFTW3 package [56].

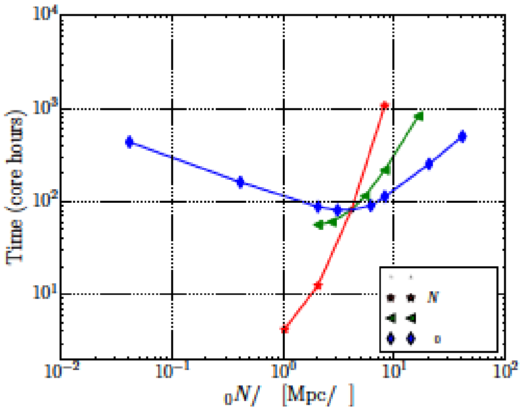

Figure 17. Dependence of the CPU core time required for the 2D Schrödinger-Poisson simulations on the simulation parameters $\kappa_0 \propto \hbar$, N and L. The figure shows variations around the fiducial values.

In figure 17 we present the dependence of the simulation time (in core hours) on κ_0, L and N for the 2D case. Increasing N has a twofold impact on the computational time: First, the time for each discrete Fourier transformation increases. Second, more non-linear scales are populated, increasing the argument of the potential rotations U_V. This requires to decrease the time step Δs, as discussed in section 3.2. Reducing the box size L also has similar effects on U_V (note that we use the combination $\kappa_0 N/L$ on the horizontal axis in figure 17). Since $\arg(U_V) \propto 1/\kappa_0$ and $\arg(U_K) \propto \kappa_0$, extreme values of κ_0 also reduce the time step and correspondingly lead to an increase in computational time.

E The 1D case

In this appendix, we present results for the one-dimensional case. As pointed out in the main text, even though the maximal possible resolution in the 1D case is the highest, the (sampling) noise is very large due to the small number or modes. Nevertheless, we find it instructive to consider the 1D case for studying the convergence when increasing the resolution.

In figure 18 we show the overdensity field at three different redshifts, for a simulation with $L = 1000$ Mpc/h, $\kappa_0 = 1\,\mathrm{Mpc}^2$ and $N = 2^{17}$ – a substantial increase compared with both 2D and 3D cases. It is possible to see that a small initial fluctuation, for instance, at $x = 250$ Mpc/h, evolves to form an overdense region.

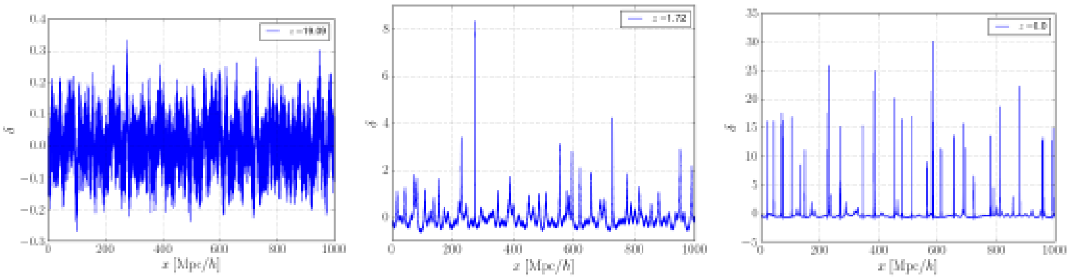

Figure 18. Overdensity field in the 1D SP system at three different redshifts.

In the left panel of figure 19, we show the overall amplitude loss in the 1D case, defined as in equation (4.3) together with the averaged relative phases that indicate the failure of the grid to resolve the highest velocities. In the right panel of figure 19, we show the PDF obtained for different values of N. For $N \gtrsim 2^{14}$, the PDF starts to converge. We also run simulations with larger volume and larger κ to confirm the reduction of a power loss in these cases. We average over 10 different initial conditions to reduce noise and finite volume effects.

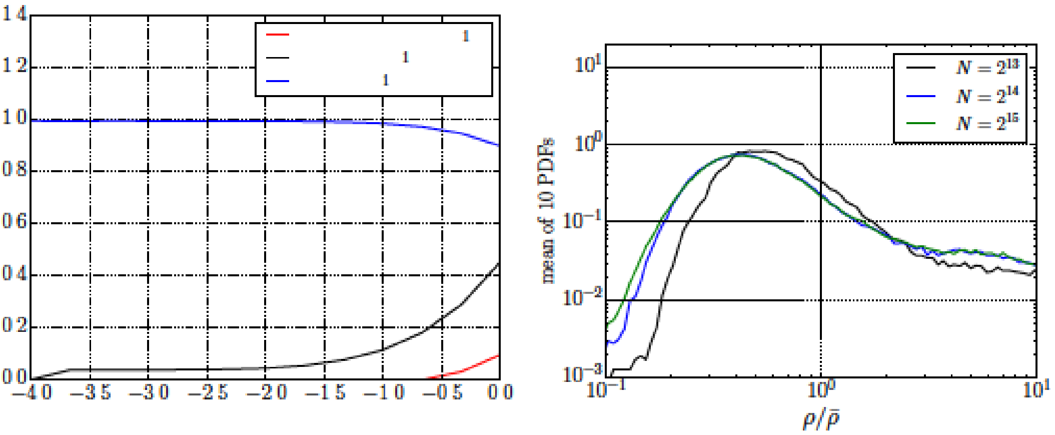

Figure 19. Left: The plot shows the suppression factor A^2, the average of the relative phases and the fraction of large relative phases ($> \pi/4$) versus time (analogous to Fig. 7 for 2D). Right: PDF for different grid sizes N averaged over 10 different initial conditions.

References

[1] **Planck** Collaboration, N. Aghanim *et al.*, “Planck 2018 results. VI. Cosmological parameters,” `arXiv:1807.06209 [astro-ph.CO]`.

[2] **BOSS** Collaboration, S. Alam *et al.*, “The clustering of galaxies in the completed SDSS-III Baryon Oscillation Spectroscopic Survey: cosmological analysis of the DR12 galaxy sample,” *Mon. Not. Roy. Astron. Soc.* **470** no. 3, (2017) 2617–2652, `arXiv:1607.03155 [astro-ph.CO]`.

et al.

Astrophys. J. Suppl.
arXiv:1707.09322 [astro-ph.GA]

et al.
Astrophys. J. Suppl. arXiv:1801.03181
[astro-ph.IM]

et al.

Phys. Rev. arXiv:1810.02499 [astro-ph.CO]

et al.
arXiv:1909.11006 [astro-ph.CO]

et al.
Living Rev. Rel.
arXiv:1206.1225 [astro-ph.CO]

et al.
arXiv:1907.10688 [astro-ph.IM]

et al.
Publ. Astron. Soc.
Jap. arXiv:1206.0737 [astro-ph.CO]

et al.
arXiv:0912.0201 [astro-ph.IM]

Annalen Phys.
arXiv:1210.0544 [astro-ph.CO]

Mon. Not. Roy.
Astron. Soc. arXiv:astro-ph/0505010 [astro-ph]

JCAP arXiv:1503.05920
[astro-ph.CO]

Astrophys. J. Suppl. arXiv:astro-ph/9509047
[astro-ph]

Phys. Rept.
arXiv:astro-ph/0112551 [astro-ph]

Phys. Rev. arXiv:astro-ph/0509418 [astro-ph]

Phys. Rev. arXiv:0905.0479
[astro-ph.CO]

JCAP arXiv:1004.2488
[astro-ph.CO]

JCAP
arXiv:1205.5274 [astro-ph.CO]

JHEP arXiv:1206.2926
[astro-ph.CO]

JCAP arXiv:1309.3308 [astro-ph.CO]

JCAP arXiv:1507.02255
[astro-ph.CO]

arXiv:1906.00997 [astro-ph.CO]

Phys. Rept.
arXiv:astro-ph/0206508 [astro-ph]

Phys. Rev. Lett. arXiv:1602.01784 [astro-ph.CO]

Phys. Rev. arXiv:1609.02544
[astro-ph.CO]

JCAP arXiv:1506.03088
[astro-ph.CO]

Mon. Not. Roy. Astron. Soc. arXiv:1404.2280
[astro-ph.CO]

Mon. Not. Roy. Astron. Soc. arXiv:1812.07489
[astro-ph.CO]

arXiv:1909.00008 [astro-ph.CO]

Phys. Rev. Lett.

arXiv:astro-ph/0003365 [astro-ph]

Phys. Rev. arXiv:1610.08297 [astro-ph.CO]

Astrophys. J.

Phys. Rev. arXiv:1403.5567 [astro-ph.CO]

Nature Phys.
arXiv:1406.6586 [astro-ph.GA]

JCAP arXiv:1710.04846 [astro-ph.CO]

Phys. Rev.
arXiv:1711.00140 [astro-ph.CO]

Phys. Rev.
arXiv:1801.03507 [astro-ph.CO]

Phys. Rev. arXiv:1804.09647 [astro-ph.CO]

arXiv:1810.01915 [astro-ph.CO]

arXiv:1812.05633 [astro-ph.CO]

Phys. Rev. arXiv:0809.4606 [astro-ph]

JCAP arXiv:1307.3220 [astro-ph.CO]

JCAP
arXiv:1509.07886 [hep-th]

JCAP arXiv:1607.03453 [astro-ph.CO]

JCAP arXiv:1812.06891 [astro-ph.CO]

Mon. Not. Roy. Astron. Soc. arXiv:1412.2133 [astro-ph.CO]

Mon. Not. Roy. Astron. Soc.

Progress of Theoretical Physics Supplement
http://oup.prod.sis.lan/ptps/article-pdf/doi/10.1143/PTPS.98.109/5366098/98-109.pdf
https://doi.org/10.1143/PTPS.98.109

Astron. Astrophys.

Mon. Not. Roy. Astron. Soc. arXiv:1603.05253 [astro-ph.CO]

Phys. Rev. arXiv:astro-ph/0205436 [astro-ph]

arXiv:1104.2932 [astro-ph.IM]

J. Korean Astron. Soc. arXiv:1112.1754 [astro-ph.CO]

Mon. Not. Roy. Astron. Soc. arXiv:1710.09881 [astro-ph.CO]

Proceedings of the IEEE